Electron phase-space control in photonic chip-based particle acceleration

https://doi.org/10.1038/s41586-021-03812-9

Received: 29 January 2021

Accepted: 7 July 2021

R. Shiloh[1,4]✉, J. Illmer[1,4]✉, T. Chlouba[1,4], P. Yousefi[1], N. Schönenberger[1,2], U. Niedermayer[3], A. Mittelbach[1] & P. Hommelhoff[1,2]✉

Particle accelerators are essential tools in science, hospitals and industry[1–6]. Yet their costs and large footprint, ranging in length from metres to several kilometres, limit their use. The recently demonstrated nanophotonics-based acceleration of charged particles can reduce the cost and size of these accelerators by orders of magnitude[7–9]. In this approach, a carefully designed nanostructure transfers energy from laser light to the particles in a phase-synchronous manner, accelerating them. To accelerate particles to the megaelectronvolt range and beyond, with minimal particle loss[10,11], the particle beam needs to be confined over extended distances, but the necessary control of the electron beam's phase space has been elusive. Here we demonstrate complex electron phase-space control at optical frequencies in the 225-nanometre narrow channel of a silicon-based photonic nanostructure that is 77.7 micrometres long. In particular, we experimentally show alternating phase focusing[10–13], a particle propagation scheme for minimal-loss transport that could, in principle, be arbitrarily long. We expect this work to enable megaelectronvolt electron-beam generation on a photonic chip, with potential for applications in radiotherapy and compact light sources[9], and other forms of electron phase-space control resulting in narrow energy or zeptosecond-bunched beams[14–16].

Particle accelerators have enabled the discovery of the fundamental constituents of matter, exemplified by the recent identification of the Higgs particle[1,2]. In addition, they drive modern light sources such as synchrotrons and free electron lasers, which allow unrivalled insights into structural biology and material science[3,4]. Metre-long versions of accelerators provide radiation in modern hospitals for cancer treatment[5,6].

Accelerators accelerate charged particles while, at the same time, confining them transversally. This is challenging because the larger the acceleration, the larger the forces that disperse the beam, reflecting Earnshaw's theorem[10,17]. In the radiofrequency (RF) accelerators currently used, methods have been found to accelerate and confine the particle beam[10].

Recently, laser-based electron acceleration has been demonstrated based on efficient momentum transfer from strong optical nearfields generated at nanophotonic dielectric structures[7,8]—first proposed in 1962[18,19] and today termed dielectric laser acceleration (DLA)[9]. This is the counterpart of classical RF acceleration but at a factor of ~10,000 larger driving frequencies and hence in a structure with feature sizes smaller by the same factor. Intriguingly, at optical frequencies, dielectric structures can withstand peak fields roughly a factor of 100 larger than their metallic RF cavities counterparts. A damage threshold of $9\ \mathrm{GV\ m^{-1}}$ and an accelerating field of $1.8\ \mathrm{GV\ m^{-1}}$ have already been demonstrated in DLA[20]. Similarly, all functional elements required in any particle accelerator have been demonstrated in DLA, including acceleration[7,8,20,21], deflection[22,23] and focusing[23–25] with purely optical forces, as well as waveguide-fed DLA[26].

The small size of DLA features also reflects DLA's largest limitation: the acceleration channel aperture is orders of magnitudes smaller than that of RF accelerators. Hence, DLA bunch charges will always be much smaller than RF accelerator bunch charges. Yet, mainly because of high-repetition-rate lasers powering future dielectric laser accelerators, they are now even being discussed in the context of future linear colliders with their demanding luminosity and (average) current demands[27]. Clearly, a greatly increased pulse charge will be needed for DLA to succeed, in addition to the extended beam control discussed here.

To our knowledge, the longest DLA structure hitherto used for subrelativistic electrons was 13.2 μm long[14]. To greatly increase the acceleration length, active control schemes need to be devised to confine a beam and prevent particle loss[28]. We show here that with complex phase-space control, we can transport a beam through a 77.7-μm-long structure. Without experiencing net acceleration, electrons are actively propagated through the DLA structure with the help of optical nearfield forces. Low-loss transport is essential because without it the best acceleration will not lead to noticeable electron currents, let alone to a power-efficient accelerator[9]. For transport, too, Earnshaw's theorem imposes severe limitations: continuous focusing in all spatial directions is prohibited. Alternating phase focusing (APF) circumvents this by repeatedly alternating the focusing directions and allowing defocusing in the other direction[10,12,13,19,29].

---

[1] Physics Department, Friedrich-Alexander-Universität Erlangen-Nürnberg (FAU), Erlangen, Germany. [2] Max Planck Institute for the Science of Light, Erlangen, Germany. [3] Technische Universität Darmstadt, Institute for Accelerator Science and Electromagnetic Fields (TEMF), Darmstadt, Germany. [4] These authors contributed equally: R. Shiloh, J. Illmer, T. Chlouba. ✉e-mail: roy.shiloh@fau.de; johannes.i.illmer@fau.de; peter.hommelhoff@fau.de

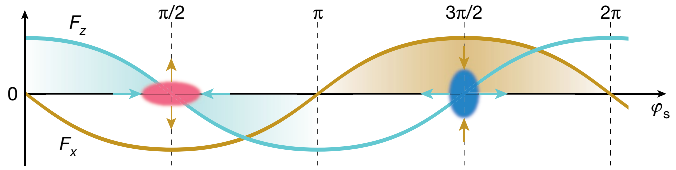

Fig. 1 | Forces acting as a function of the synchronous phase φ_s. The forces acting on a charged particle copropagating with the optical nearfield mode according to equation (1), as a function of the particle's position inside of the mode, the synchronous phase φ_s. The longitudinal force F_z is shown in cyan. The orange curve shows the transverse force F_x acting on a particle at negative transverse (x) position. The force is flipped for positive x values, leading to focusing or defocusing behaviour, indicated by the arrows. Around $\varphi_s = \pi/2$, the pulse is transversally defocused but longitudinally focused (D phase), around $\varphi_s = 3\pi/2$, it is transversally focused but longitudinally defocused (F phase). The colour gradient indicates the strength of the respective focusing force.

The force on the synchronous electron can be written as[13,23]

$$\mathbf{F} = \frac{qc}{\beta\gamma} C_C \left(\hat{\mathbf{x}} \frac{1}{\gamma} \sinh(k_x x) \sin\varphi_s + \hat{\mathbf{z}} \cosh(k_x x) \cos\varphi_s \right) \qquad (1)$$

where q is the electron charge, c the speed of light, β the velocity of the electron in units of c, γ the Lorentz factor, C_C the excitation coefficient of the driving mode, k_x the fundamental wavenumber of the DLA structure and φ_s the synchronous phase (Fig. 1). The particles propagate in the $\hat{\mathbf{z}}$-direction, where $\hat{\mathbf{x}}$ is the transverse direction parallel to the substrate (Fig. 2, 3), and the particle velocity and the optical mode velocity are identical, that is, the system operates in the phase-synchronous regime[10]. For this reason, no explicit time dependence shows up in equation (1), although it is implicitly reflected by the synchronous phase φ_s: The synchronous electron experiences a constant synchronous force, which depends strongly on the time the electron is injected into the optical mode (Fig. 1). The synchronous phase and the incident laser phase have a fixed phase relation for purely periodic synchronous transport structures. However, the synchronous phase can be changed easily and almost instantaneously by introducing a gap in the periodic nanostructure, leading to a jump in the optical phase of the nearfield mode acting on the propagating electrons.

For an electron close to the central axis ($x = 0$), we can plot the force components depending on φ_s as depicted in Fig. 1. For $\varphi_s = 3\pi/2$, the electron experiences a transversely focusing, longitudinally defocusing force (F phase for short), whereas for $\varphi_s = \pi/2$, the electron experiences a transversely defocusing, longitudinally focusing force (D phase). By variation of φ_s, we can repeatedly switch between the F and D phases (Fig. 2). The DLA structure is thus separated into F and D macro cells, realizing a FODO lattice, where O stands for no force (drift). It is well known that FODO lattices may lead to full confinement of the electron pulses[11]. Here, we choose the narrow transverse and the longitudinal direction as two directions out-of-phase by π/2. Because the nanophotonic pillars are 3 μm high (Fig. 3), we do not require forces along the y-direction (see Methods). Extension to a full three-dimensional (3D) confinement can be readily achieved if needed[29].

Figure 2 shows the behaviour of electrons in transverse phase space (x–x') and longitudinal phase space (Δs–$\Delta s'$) for one FODO lattice period. Here, x describes the particle position transversally off the centre line, and x' is the electron's angle with respect to straight propagation. Δs describes the deviation from the synchronous particle (which propagates at the synchronous phase), and $\Delta s'$ the longitudinal momentum of change. Figure 2a–d shows that when the electron is focused transversally, it is debunched (defocused) longitudinally, and vice versa: Starting at $z = 0$ ($\varphi_s = \pi/2$ in Fig. 2), the transverse size of the beam (x) decreases because x' is negative for positive x and vice versa (Fig. 2b)—the beam is converging. Simultaneously, the forces in this D macro cell counter this momentum, allowing the beam to reach a minimum at the centre of the macro cell before diverging again. After the phase jump to $\varphi_s = 3\pi/2$, the beam size (x) continues to grow, owing to x' being negative for negative x and vice versa. However, the optical force again counters this behaviour, allowing the beam to reach a point of maximum size in x before starting to focus again. This procedure repeats in each FODO lattice period. In parallel, the same happens in the longitudinal direction, but shifted by half a period (Fig. 2c, d).

So far, we have discussed the behaviour of an electron bunch occupying a small phase section to illustrate the dynamics. The experimental situation is more complex because the electrons arrive at the structure in an unbunched fashion[30]; hence all phases are occupied. However, the APF effect in a pure transport structure works for all initial phases[13].

The photonic nanostructures used in the experiment consist of 3-μm-high pillar pairs etched in monocrystalline silicon with an open channel width of 225 nm (Fig. 3). The high-contrast structure (Fig. 3a) comprises 10 macro cells, each consisting of 12 silicon pillar pairs. The required phase jump is realized with a 589-nm-long drift gap between the macro cells. With this structure, we show successful beam transport over a total structure length of 77.7 μm, entailing 10 π-phase jumps, 10 macro cells and thus 5 FODO lattice periods.

The experimental set-up is described under Methods. Briefly, a 28.4-keV pulsed electron beam is generated in a modified commercial scanning electron microscope (SEM). The ~600-fs-long electron pulses are focused into the channel of the photonic nanostructure. After the interaction, the electron beam energy is measured with a magnetic spectrometer. The nanostructure is driven with femtosecond laser pulses of 1.93 μm central wavelength and 680 fs pulse duration, focused cylindrically to a spot size of 94 μm (1/e^2 radius) along the nanostructure channel and 14 μm along the pillar height. The laser field polarization points along the travel direction of the electrons, and the temporal overlap between laser and electron pulses is controlled by a delay stage in the laser beamline.

We measure the normalized electron current (see Methods) through the high-contrast structure as a function of the peak optical field strength. With increasing laser intensity, more electrons are guided, and the current increases steadily (Fig. 4a). At a peak field strength of 727 MV m^{-1} ± 76 MV m^{-1}, a factor of 2.67 ± 0.05 more electrons are transported through than without laser, where the current decreases along the structure (Fig. 4e). Numerical particle tracking simulations, explained in detail in the Methods section, fit the experimental behaviour well (solid line in Fig. 4a).

To show that too large a field strength leads to over-focusing and hence an electron current that again decreases, we would need to increase the field strength to above 800 MV m^{-1} in this structure, but for such large field strengths laser-induced damage sets in. We can design a structure with longer macro-cell dimension so that optimal transport is achieved at a smaller field strength, at the cost of decreased total current transmission. This over-focusing structure is shown in Fig. 4f and Extended Data Fig. 3. Here we use 24 pillar pairs per macro cell such that the electrons experience the same phase (D or F) for twice as long. This second type of APF structure contains four macro cells and two half cells at the beginning and the end, with a total length of 76.2 μm. The optimal transport field strength is 325 MV m^{-1}. For larger field strengths, the electrons are over-focused, resulting in a loss of electrons, as observed in Fig. 4c. For peak fields larger than 550 MV m^{-1}, the normalized current falls below 1, indicating that now the laser fields actively destroy the beam rather than preventing it from crashing into the channel walls.

In Fig. 4b we show an electron energy spectrum as a function of the temporal overlap between laser pulses and electron pulses in the high-contrast structure. For maximum overlap, the largest electron

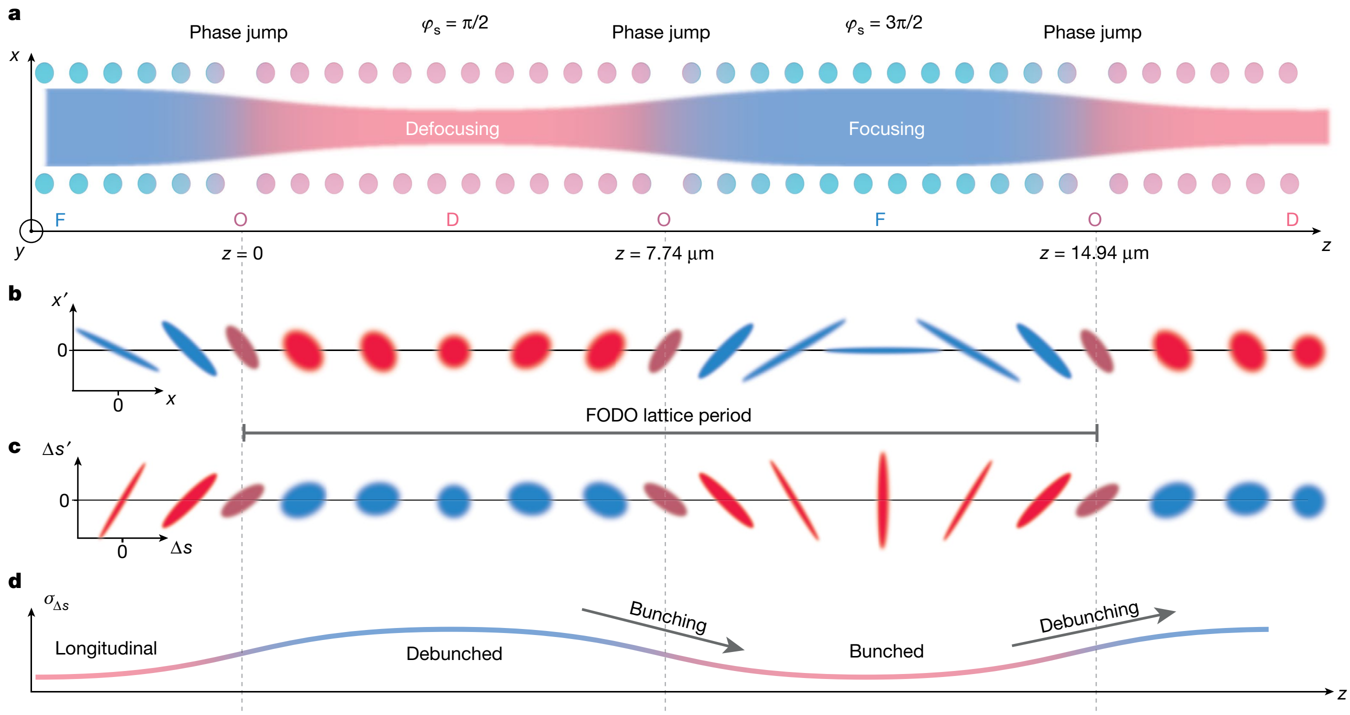

Fig. 2 | Complex optical electron phase-space control in alternating phase focusing. a, Sketch of the electron-beam envelope (coloured band) under the influence of the optical nearfield generated by the dielectric nanostructure. Filled circles indicate nanopillars extruded out of plane (*y*-direction). **a**, **b**, Evolution of a particle ensemble in transverse phase space relative to the structure layout: The electron distribution at $z = 0$ is compressed in transverse phase space (*x* extent decreasing), while in this D cell transversally defocusing forces already act on the electrons. The point of minimum transverse size is reached in the middle of the first macro cell ($z = 3.87$ µm). At $z = 7.74$ µm, a gap in the structure leads to a jump in the synchronous phase φ_s between electrons and optical nearfield so that the particles now experience transverse focusing forces (F cell). **c**, **d**, The longitudinal forces, 90° out of phase relative to the transverse forces, act similarly on the longitudinal phase-space distribution: the pulse length ($\sigma_{\Delta s}$) maximum in the longitudinal direction coincides with the minimal extent in the transverse direction and vice versa. The net effect is a confinement of the beam both transversally and longitudinally. For illustration purposes, the particles depicted occupy a small initial phase volume.

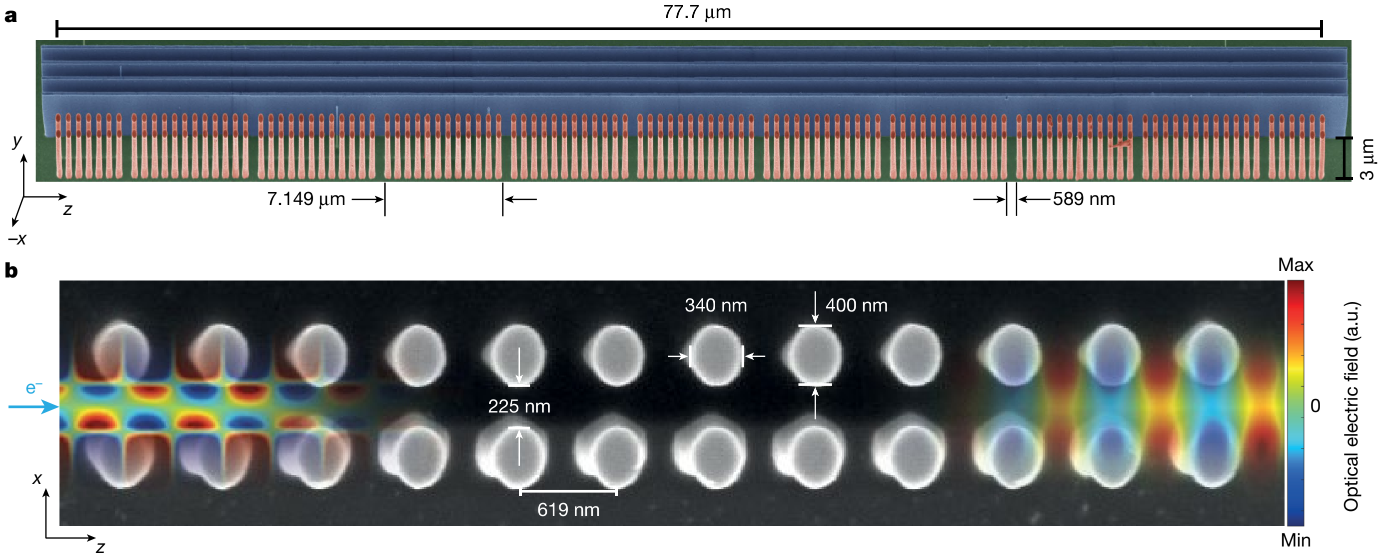

Fig. 3 | Silicon photonic nanostructure for phase-space control. a, SEM image of the 10 macro cell APF structure (high-contrast structure), coloured for clarity. Each full macro cell is 7.149 µm long and is separated from its neighbour cell by a 589-nm-wide gap. The two half cells at the beginning and end ensure that an unbunched beam is optimally coupled in and out of the structure (see Methods). The total structure length is 77.7 µm. The pulsed laser beam impinges on the nanostructure along the *x*-direction. A distributed Bragg reflector (blue) placed behind the pillar structure reflects the laser light back to create a symmetric field distribution[31]. **b**, Top view of one macro cell. The pillars consist of elliptic silicon cylinders with axes 400 nm and 340 nm long, and a height of 3 µm. The distance between pillars is 619 nm. Dimensions have to be accurate to 20 nm for efficacy of the structure (see Methods). Electrons (light blue arrow) are injected from the side. The colour superimposed on the left shows a snapshot of the electric field component exerting transverse forces (along *x*) on the electrons, while the colour on the right displays the electric field component in longitudinal *z*-direction.

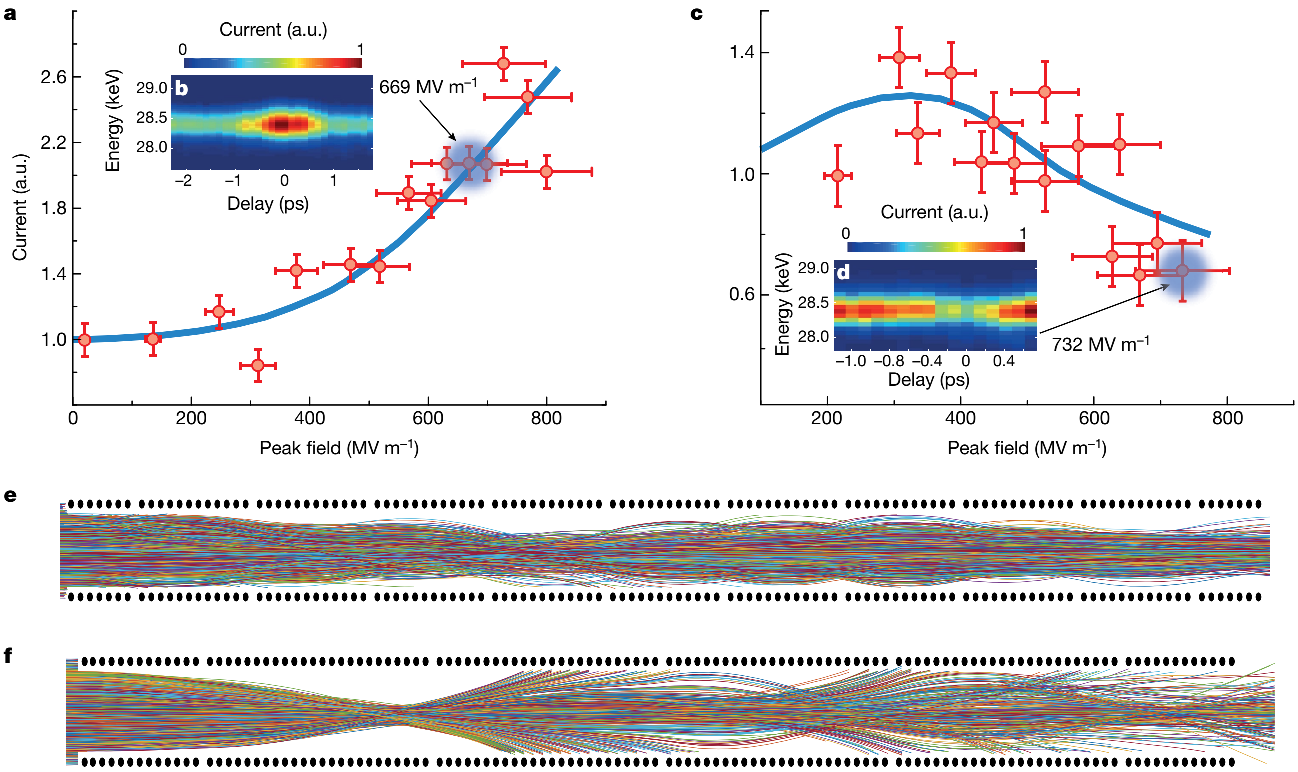

Fig. 4 | Experimental verification of the APF scheme. a, Current after the high-contrast structure as function of the peak optical field. Red points, experimental data; blue curve, particle tracking simulation results. The current increases from 1 (laser off) with increasing field strength up to a maximum value of 2.67 ± 0.05. **b**, Time delay scan between electron and laser pulses of the spectrally resolved current at 669 MV m^{-1} ± 70 MV m^{-1}. Clearly, the largest current is observed for maximum temporal overlap (zero time delay). **c**, As in **a** but now for the over-focusing structure. Over-focusing sets in for fields larger than 300 MV m^{-1}. The current drops to below 1 for fields larger than 550 MV m^{-1}. **d**, Same as in **b** for the over-focusing structure at 732 MV m^{-1} ± 76 MV m^{-1}. Now, the largest electron loss happens at maximum overlap. **e**, **f**, Example particle trajectories in the high-contrast structure, **e**, and in the over-focusing structure, **f**. Excellent beam transport is observed in **e**, while over-focusing is visible in **f**. The colours in **e** and **f** are chosen to discern individual trajectories for presentation purposes. Error bars mark the measured value ±1 s.d.—see Methods for details.

count rate is observed, and this drops with decreasing temporal overlap. The spectral width remains minimal as predicted by our numerical simulations. Figure 4d shows the same temporal overlap scan for the overfocusing structure at 732 MV m^{-1} ± 76 MV m^{-1} peak electric field. Here we observe a minimum in the electron count rate. The advantage of the APF scheme is apparent: particles can be transported while confined in these narrow channels, all the while keeping the energy spread minimal.

Figure 4e depicts simulated example particle trajectories in the case of optimal guiding in the high-contrast structure. Some particles are lost at in-coupling, but then the forces acting on the remaining particles are ideal to transport all of them through the structure. The simulated electron beam parameters are consistent with the experimental ones: The normalized input emittance was determined previously as 100 pm-rad[30,31]. In contrast, Fig. 4f shows an example of particle trajectories for the over-focusing case. Because the transverse forces acting on the particles are too strong, the focusing force is no longer matched to the phase jump intervals, so the electrons gain too large a transverse momentum, and minimal-loss guiding cannot be maintained.

For both structure types, experimental results agree well with our particle tracking simulations. In addition to the transverse dynamics, the APF scheme inevitably also induces longitudinal phase-space effects. These result from the selective energy modulation that the electrons undergo as they are transported through the structure and manifest as bunching (Fig. 2c, d). Because this is periodic with the pillar period of 619 nm, a train of sub-optical short bunches of electrons is generated every 3.23 fs (half an optical period). The generation of bunch trains of electrons can also be attained after propagation through a simpler uniform energy modulation structure plus ballistic propagation[14,15]. In that case, the electrons first gain a large energy spread and are then merely rotated by 90° in phase space. Specifically designed APF bunchers can compensate the created energy spread[13,16].

In conclusion, we have experimentally demonstrated ten-in-a-row well-controlled coupled transverse and longitudinal phase-space rotations—at optical frequencies in a nanophotonic structure on a chip. In our alternating phase focusing scheme, we were able to transport an electron beam over a length of 77.7 μm in a 225-nm-wide channel. Refinement of the FODO cell design will allow combined confinement and net acceleration[13,29]. Because this scheme is scalable, we can now extend dielectric laser acceleration to long photonic structures. In particular, one could start with electrons at 30 keV and accelerate them up to 1 MeV (see Methods). Assuming an average acceleration gradient of 1 GeV m^{-1}, 1 MeV is achievable on a 1-mm-long chip. Such a particle accelerator on a chip could result in compact light sources[32], potentially even compact free-electron lasers[9,28] and high-energy particle colliders[27], and could also be used in miniature catheterized radiation therapy devices. Similarly, the high degree of phase-space control will open the door to extreme electron-beam parameters including narrow-energy beams[16] as well as bunching down into the zeptosecond realm[14].

Online content

Any methods, additional references, Nature Research reporting summaries, source data, extended data, supplementary information, acknowledgements, peer review information; details of author contributions and competing interests; and statements of data and code availability are available at https://doi.org/10.1038/s41586-021-03812-9.

1. Aad, G. et al. A particle consistent with the Higgs boson observed with the ATLAS detector at the large hadron collider. *Science* **338**, 1576–1582 (2012).
2. Chatrchyan, S. et al. A new boson with a mass of 125 GeV observed with the CMS experiment at the large hadron collider. *Science* **338**, 1569–1575 (2012).
3. Focus: Synchrotron techniques. *Nat. Rev. Mater*. https://www.nature.com/collections/vjzmtcbvzy (2018).
4. Bucksbaum, P., Möller, T. & Ueda, K. Frontiers of free-electron laser science. *J. Phys. At. Mol. Opt. Phys.* **46**, 160201 (2013).
5. Karzmark, C. J. Advances in linear accelerator design for radiotherapy. *Med. Phys.* **11**, 105–128 (1984).
6. Podgorsak, E. B. *Radiation Oncology Physics: A Handbook for Teachers and Students* (International Atomic Energy Agency, 2005).
7. Breuer, J. & Hommelhoff, P. Laser-based acceleration of nonrelativistic electrons at a dielectric structure. *Phys. Rev. Lett.* **111**, 134803 (2013).
8. Peralta, E. A. et al. Demonstration of electron acceleration in a laser-driven dielectric microstructure. *Nature* **503**, 91–94 (2013).
9. England, R. J. et al. Dielectric laser accelerators. *Rev. Mod. Phys.* **86**, 1337–1389 (2014).
10. Wangler, T. P. *RF Linear Accelerators* 2nd edition (Wiley-VCH, 2008).
11. Chao, A. W., Mess, K. H., Tigner, M. & Zimmermann, F. *Handbook of Accelerator Physics and Engineering* 2nd edition (2013).
12. Courant, E. D. & Snyder, H. S. Theory of the alternating-gradient synchrotron. *Ann. Phys.* **3**, 1–48 (1958).
13. Niedermayer, U., Egenolf, T., Boine-Frankenheim, O. & Hommelhoff, P. Alternating-phase focusing for dielectric-laser acceleration. *Phys. Rev. Lett.* **121**, 214801 (2018).
14. Schönenberger, N. et al. Generation and characterization of attosecond microbunched electron pulse trains via dielectric laser acceleration. *Phys. Rev. Lett.* **123**, 264803 (2019).
15. Black, D. S. et al. Net acceleration and direct measurement of attosecond electron pulses in a silicon dielectric laser accelerator. *Phys. Rev. Lett.* **123**, 264802 (2019).
16. Niedermayer, U. et al. Low-energy-spread attosecond bunching and coherent electron acceleration in dielectric nanostructures. *Phys. Rev. Appl.* **15**, L021002 (2021).
17. Panofsky, W. K. H. & Wenzel, W. A. Some considerations concerning the transverse deflection of charged particles in radio-frequency fields. *Rev. Sci. Instrum.* **27**, 967 (1956).
18. Shimoda, K. Proposal for an electron accelerator using an optical maser. *Appl. Opt.* **1**, 33–35 (1962).
19. Lohmann, A. Electron acceleration by light waves. *IBM Tech. Note* **5**, 169–182 (1962).
20. Cesar, D. et al. High-field nonlinear optical response and phase control in a dielectric laser accelerator. *Commun. Phys.* **1**, 46 (2018).
21. Leedle, K. J., Fabian Pease, R., Byer, R. L. & Harris, J. S. Laser acceleration and deflection of 96.3 keV electrons with a silicon dielectric structure. *Optica* **2**, 158–161 (2015).
22. Kozák, M. et al. Optical gating and streaking of free electrons with sub-optical cycle precision. *Nat. Commun.* **8**, 14342 (2017).
23. Leedle, K. J. et al. Phase-dependent laser acceleration of electrons with symmetrically driven silicon dual pillar gratings. *Opt. Lett.* **43**, 2181 (2018).
24. McNeur, J. et al. Elements of a dielectric laser accelerator. *Optica* **5**, 687–690 (2018).
25. Black, D. S. et al. Laser-driven electron lensing in silicon microstructures. *Phys. Rev. Lett.* **122**, 104801 (2019).
26. Sapra, N. V. et al. On-chip integrated laser-driven particle accelerator. *Science* **367**, 79–83 (2020).
27. Shiltsev, V. & Zimmermann, F. Modern and future colliders. *Rev. Mod. Phys.* **93**, 015006 (2021).
28. Naranjo, B., Valloni, A., Putterman, S. & Rosenzweig, J. B. Stable charged-particle acceleration and focusing in a laser accelerator using spatial harmonics. *Phys. Rev. Lett.* **109**, 164803 (2012).
29. Niedermayer, U., Egenolf, T. & Boine-Frankenheim, O. Three dimensional alternating-phase focusing for dielectric-laser electron accelerators. *Phys. Rev. Lett.* **125**, 164801 (2020).
30. Kozák, M. et al. Ultrafast scanning electron microscope applied for studying the interaction between free electrons and optical near-fields of periodic nanostructures. *J. Appl. Phys.* **124**, 023104 (2018).
31. Yousefi, P. et al. Dielectric laser electron acceleration in a dual pillar grating with a distributed Bragg reflector. *Opt. Lett.* **44**, 1520 (2019).
32. Roques-Carmes, C. et al. Towards integrated tunable all-silicon free-electron light sources. *Nat. Commun.* **10**, 3176 (2019).

Methods

Experimental set-up

A commercial SEM (Philips XL-30) was used as an electron-beam source. In our system, the Schottky emitter in the electron gun is triggered by ~150-fs-long (full-width half-maximum, FWHM) ultraviolet laser pulses at 257 nm with an energy of 6 nJ and polarized parallel to the electron propagation direction with a repetition rate of 167 kHz. The released electrons are then accelerated in the microscope column to 28.4 keV. Owing to trajectory effects[30], at the interaction point with the nanostructures, the electron pulses are estimated to be roughly 600 fs long (FWHM). The electron beam is focused to the structure entrance with a transverse beam size of ~10 nm (FWHM, measured in the normal, continuous-imaging mode). The electron energy is measured using a home-built magnetic spectrometer and a Chevron-type microchannel plate (MCP) (Extended Data Fig. 1).

The photonic structure is driven by 1.93-μm infrared laser pulses with 680-fs FWHM duration. The beam is linearly polarized along the particle propagation direction and has a cylindrical shape in order to illuminate the whole structure with $1/e^2$ radius of 94 μm and 9 μm (over-focusing structure) or 14 μm (high-contrast structure). The overlap between electron and laser pulses is achieved by using a delay stage (Extended Data Fig. 1).

In the experiment, the structure is spatially aligned using the continuous-wave imaging mode of the SEM to both laser and electron beam, such that the structure's channel and first set of pillars, along with the input aperture, are in focus. The structure is also rotated around the vector normal to the substrate to make sure that the electrons pass through the channel throughout the structure length. Slight deviations from perfect angular alignment are unavoidable, since this alignment is based on observing the electron signal scattered from the channel and picked up by the secondary-electron detector of the SEM. Owing to the geometry of the dual-pillar structure and its extremely narrow channel and aspect ratio, this signal is fairly low. Specifically, for a 78-μm-long structure with a 225-nm-wide channel, using geometrical considerations we estimate that the electron beam's angle of incidence could deviate by up to 8 mrad.

Fabrication of the photonic nanostructures

The structures were fabricated by means of electron-beam lithography from highly doped (1–5 Ω cm) <100> oriented silicon wafers. First, the wafer was spin-coated with a 400-nm-thick negative resist (Micro Resist Technology ma-N 2405), which was patterned by a 100-kV lithography machine (Raith EBPG 5200). After the resist development, the silicon wafer was etched anisotropically to a depth of 3 μm at cryogenic conditions (Oxford Instruments Plasmalab100). This procedure produced the high-contrast structures directly on the wafer substrate (Extended Data Fig. 2), which, owing to geometrical considerations, required the laser beam to have a small incidence angle (5°) to reach the structure itself (Extended Data Fig. 1b).

During the later experiments, we improved our fabrication process, with the goal of eliminating the non-zero incidence angle. With this feature the laser beam can be aligned to the structure in a much easier and more precise manner. Therefore, for the over-focusing structure we used additional fabrication steps to create a mesa (Extended Data Fig. 3), which followed the process described above for the nanophotonic structure fabrication. A 6-μm-thick layer of positive photoresist (MicroChemicals AZ4562) was deposited on the wafer and patterned using a laser lithography system (Heidelberg instruments DWL66). Following resist-development, the wafer was etched by a Bosch process to a depth of about 60 μm, and consequently the structures were then elevated by the same height above the substrate (Extended Data Fig. 3). To clean the structures from the photo-resist, the wafer is immersed in a Piranha solution for 5 min.

Structure tolerances

During these experiments, we found that the structure dimensions were critical. A variation of the thickness of all structure features of more than ±20 nm completely cancelled the desired guiding effect in terms of transmission and energy spread. This is in contrast to previous DLA measurements, where no such sensitivity was found. The strict tolerances are due to the very nature of this exceptionally long structure: The optical nearfields in the experiment have to match the expected nearfields, otherwise errors can accumulate in such a long structure and jeopardize its efficacy.

Particle tracking simulations

The electromagnetic fields were calculated using the Ansys Lumerical FDTD software in 2D. In this simulation, the Gaussian laser beam waist radius was set to 90 μm ($1/e^2$), and the Gaussian pulse length to 680 fs (FWHM) at 1.93 μm central wavelength. The beam is incident perpendicular to the nanostructure, and the waist was set to intersect with the channel symmetry axis ($x = 0$ in the main text; see Fig. 3, for instance).

The numerically obtained fields were then loaded into the full 3D particle tracking software General Particle Tracer (Pulsar Physics). The electron-beam parameters were transverse normalized emittance 100 pm-rad, beam diameter 655 nm FWHM and a duration of 400 fs (FWHM). The pulse length chosen in simulation gave the best fit to the experimental data; it is reasonable to assume that in experiment, unlike in simulation, the electron pulse shape is not strictly Gaussian and instead depends heavily on trajectory effects[30]. The beam divergence half-angle was measured in experiment (using a knife-edge) to be roughly 0.5–1 mrad. We have used 0.5 mrad in our simulations.

For illustrative purposes, the trajectories shown in Fig. 4e, f depict electron pulses that are 0.001 fs in duration. With this illustration the trajectories simulated can be directly related to the schematic explanation of the transverse APF behaviour shown in Fig. 2a. In Extended Data Fig. 4, we show more trajectory simulations. Details are discussed in the caption of that figure. We emphasize that the details of the APF scheme and hence the complex phase-space control at optical frequencies can also be clearly seen here when the trajectories are analysed as shown in the figure.

Half cells at the beginning and the end of the structure

The half macro cells appearing at the beginning and end of each of the structures are a result of the design of the FODO cell, where the incident beam is assumed to have the maximum transverse width at the input of the macro cell (see supplementary material of ref. [13]). When the FODO lattice period matches the beam envelope's period, maximum transmission of current is achieved for one specific phase. Qualitatively, and regardless of the input transverse size, the effect of the half-cells can also be understood as follows. Assuming that the structure would start with a full lattice cell and an unbunched beam, all phases relative to the laser phase would be occupied. This would result in the lattice cell acting as a full F cell for one half of all phases and a full D cell for the other. Hence, while one part of the beam would be mostly confined, the other would be mostly lost to the pillars. Instead, half a cell only applies half the effect of an F cell on one part and half the effect of a D cell on the other, resulting in a practically more symmetric particle loss, or ideally no particle loss for all phases. The half cell at the end of the structure ensures symmetry and is important for matching the resulting electron bunches to additional stages envisaged in the accelerator on a chip scheme.

Independence of guiding from the injection phase

As stated in the main text, the APF effect in a pure transport structure works for all initial injection phases[13]. The lattice is designed in a similar fashion as the usual FODO scheme[33], where in each cell the maximum beam size is located at its entrance, and the minimum is in the middle of the FODO cell. APF works for all initial phases, where half of the phases would begin by focusing and the complementary half by defocusing in the transverse plane. Therefore, the lattice acceptance is phase-dependent, and the actual beam size must be smaller than the minimum acceptance of the lattice in order to transport all phases without losses.

In our experimental (and corresponding simulation) case, the beam is not matched to the acceptance of the structure, but is larger. Hence, some particle loss is unavoidable. This can be seen in the simulation in Fig. 4e, f, and in more detail in Extended Data Fig. 4a (the loss due to defocus is particularly seen in subcell 1a).

Comparison between simulation and experimental data

In the 2D simulation, we assumed normal-angle side-illumination. Therefore, to account for the 5° laser incidence angle on the high-contrast structure, the incident peak field observed in the experiment was multiplied by a factor of 1.53 (Fresnel reflection coefficient of silicon at 5° from the substrate). This incorporates the effect of interference on the structure of one part of the incident wave and another reflected from the substrate, and leads to good agreement between simulation and experimental results.

For the electron beam, an angle of 2.8 mrad relative to the *z*-axis was used to produce the simulation curve in Fig. 4a of the main text, as it agreed best with the experimental results for the high-contrast structure. These 2.8 mrad are well within the experimental angular alignment uncertainty, as discussed under ‘Experimental set-up’ above. With an input of zero angle, the simulation curve shows a similar behaviour but at a lower contrast. The over-focusing structure results match well for zero incidence angle.

Beam current

The normalized beam current is the current flowing through the structure with laser on divided by the current exiting the structure without laser illumination. With a laser repetition rate of 167 kHz and 0.005 electrons per pulse on average here, the beam current roughly equals 133 aA. For this work, the total current was of hardly any interest. Importantly, and as shown in previous work[30], the tip can emit up to 1,000 electrons per pulse, leading to potentially 10 electrons per pulse in the structure and resulting in currents up to hundreds of femtoamperes in this SEM-based set-up. Currents orders of magnitudes larger can be achieved with a more specialized source set-up[34] not based on a commercial SEM as used here. Moreover, parallelization schemes are expected to increase the current throughput by an order of magnitude for 10 channels, or by two orders of magnitude for 100 channels, for example[35]. Because of the lithographic nature of the nanophotonic structure fabrication, multichannel structures are straightforward to produce in the cleanroom. Even 3D structures have been considered and can be produced for DLA[36].We further note that collective instabilities such as wakefield effects in these structures have recently been thoroughly investigated[37]: Even for bunch charges of up to 18,000 electrons at relativistic energies, stable modes of operation can be found. For larger bunch charges, the electron bunch will be driven apart. This can be potentially countered with the forces discussed here but is beyond the scope of this work.

In the main text, we mentioned the possibility of applying DLAs in free-electron lasers, because we see intriguing ways to increase the peak current by many orders of magnitude. Several methods could all be combined to reach peak currents in excess of 1 kA: (1) temporal pulse compression down to 1 fs or below (demonstrated in ref. [14,15]), (2) a larger nanophotonic structure driven at a larger wavelength such as 10 µm (ref. [38]), with (3) an elliptical beam shape, which can be large in the direction parallel to the pillar height, and (4) the combination of the output beams of, say, 10 nanophotonics-based accelerators, all printed on the same chip (or even 10 × 10). (5) Most importantly, we expect a large increase in electron number by going to miniaturized and custom-built electron optics, including the source[34]. Discussions of these challenges and their potential workarounds are outside the scope of this work, although many of the points discussed above are included in ref. [9].

Error calculation

In Fig. 4a, c, the uncertainty of the normalized current (vertical axis) measurement is dominated by statistical noise inherent in our optical acquisition set-up of reading the MCP (see ‘Experimental set-up’ above). From repeated calibration measurements, we estimated and placed a constant standard deviation of ±0.05 on the value of the normalized current.

The peak field uncertainty (horizontal axis) is derived from the measured elliptical spot size on the structure, and the incident power. These are related through the peak field E_{peak},

$$E_{peak} = \left(\frac{8\sqrt{\ln 2}}{\pi^{3/2}} \frac{Z_0}{\tau_p f_{\mathrm{rep}}} \frac{P_{\mathrm{avg}}}{w_{0z} w_{0y}} \right)^{1/2}, \qquad (2)$$

where Z_0 is the impedance of free space, τ_{p} the duration (FWHM) of the driving laser pulse, f_{rep} the repetition rate of the laser, P_{avg} the average incident power, and w_{0z} and w_{0y} are the elliptical Gaussian beam waists intersecting the structure along the nanostructure channel (z) and the vertical (y) direction. The beam sizes on the structure are deduced by observing the reflected beam from the structure with an auxiliary camera. However, the illumination wavelength is large relative to the structure features and most of them cannot be resolved. w_{0z} can hence be estimated with good accuracy using the phase jumps and structure edges. w_{0y} is much larger than the pillar height and is estimated by moving the sample stage and reconstructing the beam intensity profile. From this, we estimate the measurement and uncertainty $w_{0z} \pm \Delta w_{0z}$ to be 94 µm ± 4.7 µm and accordingly $w_{0y} \pm \Delta w_{0y}$ to be 9 µm ± 1.8 µm (over-focusing structure) and 14 µm ± 2.8 µm (high-contrast structure). The average laser power fluctuations ΔP_{avg} during the experiments are roughly ±3% of the power. This uncertainty is then propagated to yield the peak field and error $E_{\mathrm{peak}} \pm \Delta E_{\mathrm{peak}}$.

Electron acceleration from sub-relativistic to 1 MeV energy

An appropriately designed FODO cell will allow net acceleration of a design range of injection phases. In particular, the macro-cell length and the gap size need to be changed from those used here. Given that the electron velocity increases, the parameters have to vary along the structure. Initial structure designs for acceleration in combination with APF have been published[13,29]. For an accelerating structure with large energy gain and large particle throughput, however, extending the APF confinement to 3D is needed[29]. Then, considering the observed record accelerating field of 1.8 GV m^{-1} in DLA[20], an accelerator providing 1 MeV over 1 mm is already within reach, opening up venues to several proposed applications either near[39] or further in the future[27,40].

Accelerator beam parameters

At our subrelativistic electron energy of 28.4 keV and the given laser parameters (same as for Fig. 4e), the theoretically expected β-function[10] is roughly 42 µm, which agrees well with the simulation results and the discussion around Extended Data Fig. 4. A similar result was obtained for 1 GV m^{-1} laser field in the supplementary of ref. [13]. In our example here, as previously discussed, we transport our beam using five FODO cells and roughly 80 µm, but this length can in principle be extended indefinitely, provided that some form of refocusing is used in the vertical direction[29]. It is interesting to note that CERN’s Large Hadron Collider uses 23 FODO cells over 2,450 m in each arc. The horizontal and vertical β-functions switch between maximum values of 180 m or 30 m in a complementary fashion, depending on the beam position in the accelerator’s circumference[41].

Data availability

Source data for Fig. 4a, c are provided with the paper. The data in Fig. 4b, d that support the findings of this study are available in Zenodo with the identifier https://doi.org/10.5281/zenodo.4446542. Source data are provided with this paper.

33. Wiedemann, H. *Particle Accelerator Physics* (Springer, 2015).
34. Hirano, T. et al. A compact electron source for the dielectric laser accelerator. *Appl. Phys. Lett*. (2020).
35. Zhao, Z. et al. Design of a multichannel photonic crystal dielectric laser accelerator. *Photon. Res*. **8**, 1586–1598 (2020).
36. Staude, I. et al. Waveguides in three-dimensional photonic bandgap materials for particle-accelerator on a chip architectures. *Opt. Express* **20**, 5607–5612 (2012).
37. Egenolf, T., Niedermayer, U. & Boine-Frankenheim, O. Tracking with wakefields in dielectric laser acceleration grating structures. *Phys. Rev. Accel. Beams* **23**, 054402 (2020). 0987654321``
38. Kimura, W. D., Poaorelsky, I. V & Schächter, L. CO_2-laser-driven dielectric laser accelerator. In *2018 IEEE Advanced Accelerator Concepts Workshop (AAC)* https://doi.org/10.1109/AAC.2018.8659403 (2018).
39. Egerton, R. F. Outrun radiation damage with electrons? *Adv. Struct. Chem. Imaging* **1**, 5 (2015).
40. Cros, B. & Muggli, P. Input to the European Particle Physics Strategy Update. in *Advanced Linear Collider Study Group (ALEGRO collaboration)* (2018).
41. Brüning, O. S. et al. *LHC Design Report* CERN-2004-003-V-1 (2004).

Acknowledgements We acknowledge discussions with the members of the Accelerator on a Chip International Program (ACHIP). We thank the clean-room facility staff at the Max Planck Institute for the Science of Light for continued assistance. We acknowledge funding by the Gordon and Betty Moore Foundation (#GBMF4744), ERC grants NearFieldAtto (#616823) and AccelOnChip (#884217) and BMBF projects 05K19WEB and 05K19RDE.

Author contributions T.C. and J.I. measured the data. R.S. and U.N. designed the structures and performed simulations. P.Y. fabricated the structures. J.I., R.S. and T.C. analysed the data. N.S. and A.M. inferred stringent tolerance requirements from initial measurements. J.I., R.S. and P.H. wrote the manuscript. P.H. supervised the experiment.

Competing interests The authors declare no competing interests.

Additional information

Supplementary information The online version contains supplementary material available at https://doi.org/10.1038/s41586-021-03812-9.

Correspondence and requests for materials should be addressed to R. Shiloh, J. Illmer or P. Hommelhoff.

Peer review information *Nature* thanks James Rosenzweig, Yelong Wei and the other, anonymous, reviewer(s) for their contribution to the peer review of this work.

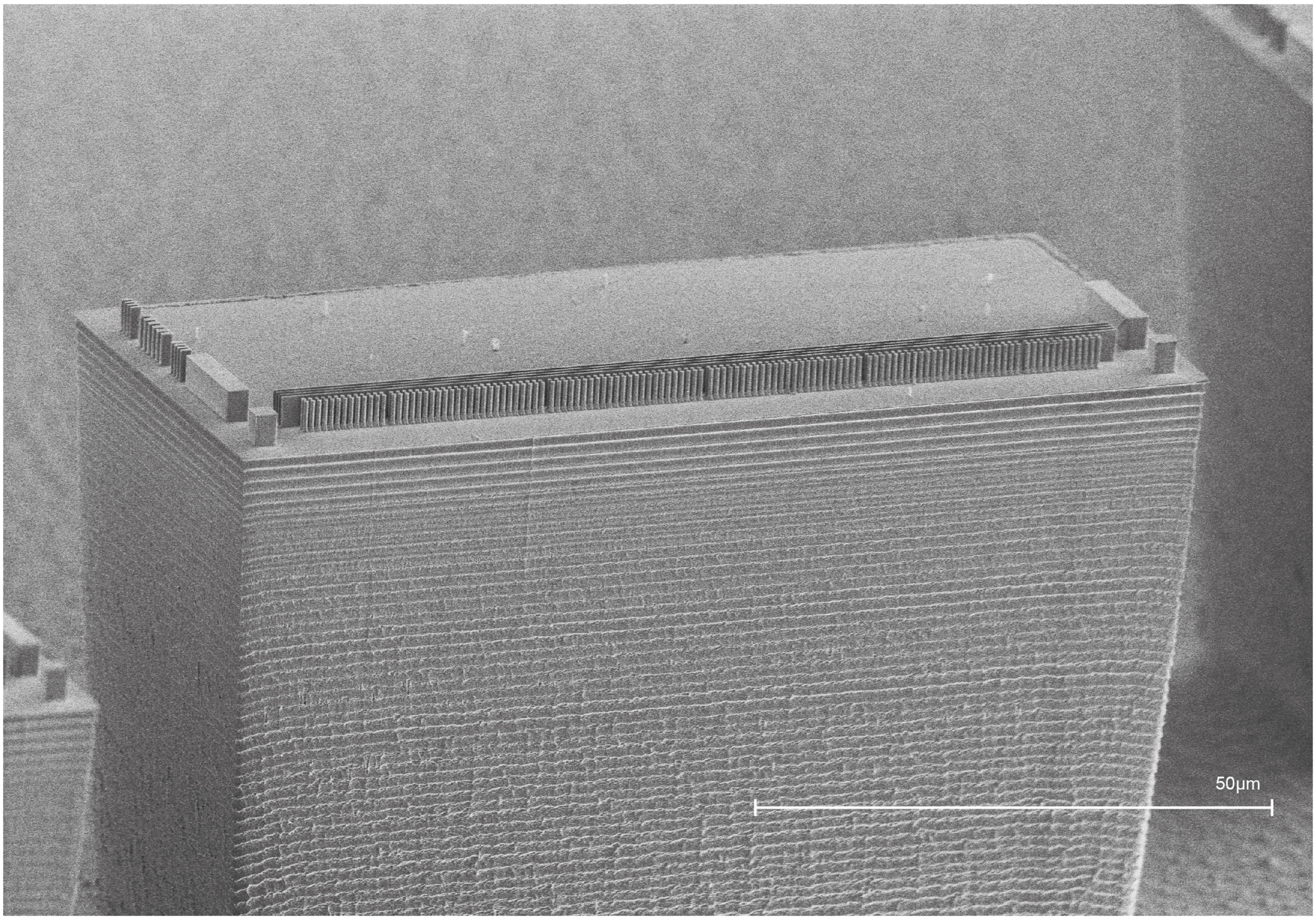

Extended Data Fig. 1 | Photonic nanostructure on top of a mesa: over-focusing structure. This SEM image shows a structure fabricated on top of a 60 µm-high mesa. The photonic structure for the over-focusing measurement is visible atop the mesa. The five gaps between the macro cells are also clearly visible. Here, 24 pillar pairs build one macro cell. Input (left) and output (right) apertures (thick blocks) are used for alignment during experiment. Additional pillars to the left of the input aperture act as markers that identify the specific structure during the experiment. The mesa allows us to focus the laser beam under 0° incidence angle from the side (see also Extended Data Fig. 1c).

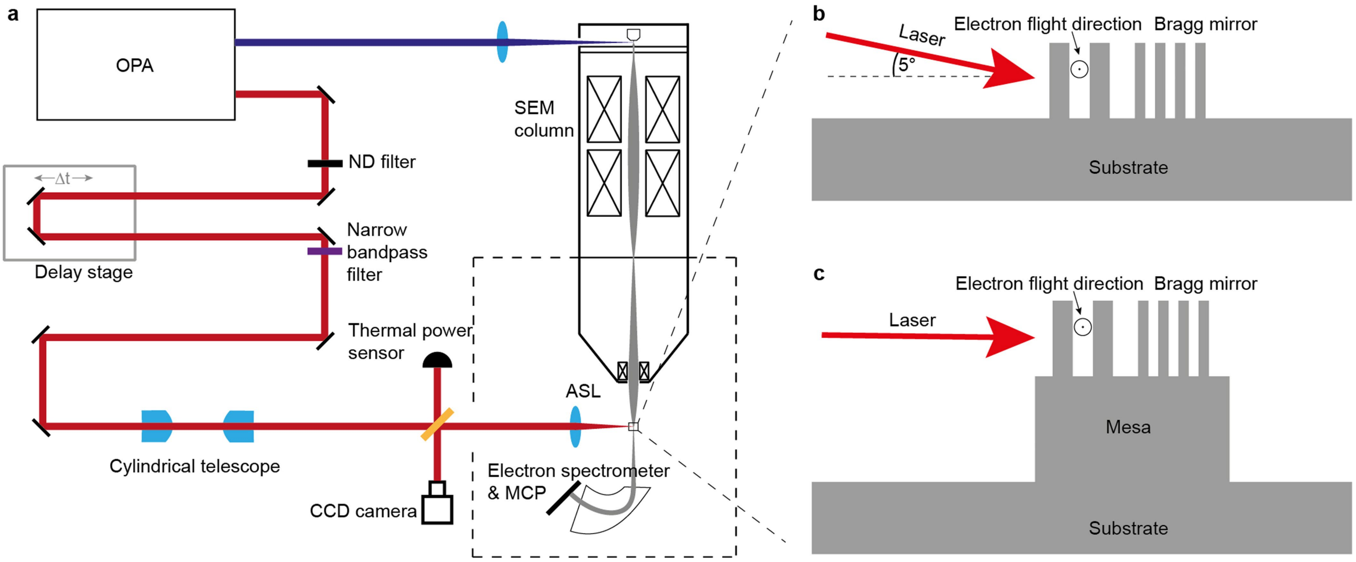

Extended Data Fig. 2 | Schematic of the experimental set-up. (a) Both IR (red) and UV (blue) laser pulses are generated with the help of an optical parametric amplifier (OPA). The UV pulses are focused onto the Schottky emitter of the SEM, where they release electron pulses. The electron pulses pass through the electron column and are focused into the nano-photonic channel. The IR pulses first pass a neutral-density (ND) filter for variable optical power attenuation before they traverse a delay stage, where the time delay between IR laser pulses and electron pulses is set. A bandpass filter limits the IR spectrum so that the laser pulses are stretched to a duration of 680 fs (FWHM). A cylindrical telescope is used to generate an elliptic laser beam with a 1:6 ratio. The beam is then split into two parts, where one part is used to monitor the power during measurements and the other is focused on the structure via an aspherical lens (ASL). The back reflection from the sample is used to align the laser beam to the structure. The electron energy is measured with a magnetic deflection spectrometer and an MCP detector with a phosphor screen, viewed from outside the vacuum chamber (indicated by the dashed line) with a CCD camera (not shown). For structures without a mesa **(b)** the incident angle of the laser beam is 5°, while for structures on top of the mesa **(c)** this angle is 0°.

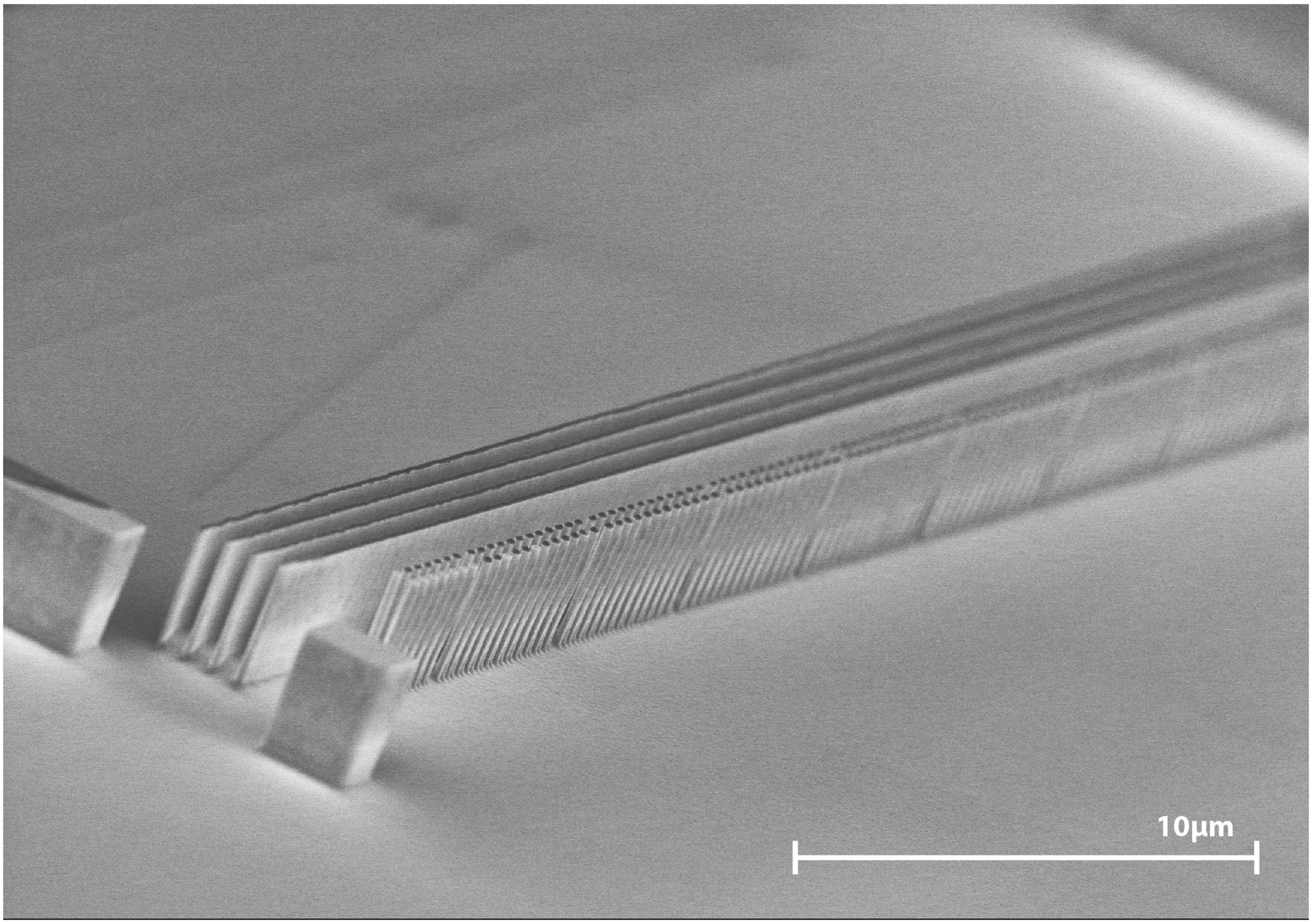

Extended Data Fig. 3 | Photonic nanostructure on flat substrate: high contrast structure. The scanning electron microscope (SEM) image shows the dual pillar transport structure for high contrast measurements. The dual pillar transport channel can be seen on the right as a colonnade structure. The four solid slabs left-above of the colonnades structure are a distributed Bragg mirror[31]. An alignment aperture is placed at the input of the structure (thick blocks). Electrons are focused into the colonnade structure, that is, into the channel between the rows of pillars. The laser beam impinges on the structure from the side, from bottom-right here, perpendicular to the pillars and with a 5° angle to the substrate (see also Extended Data Fig. 1b).

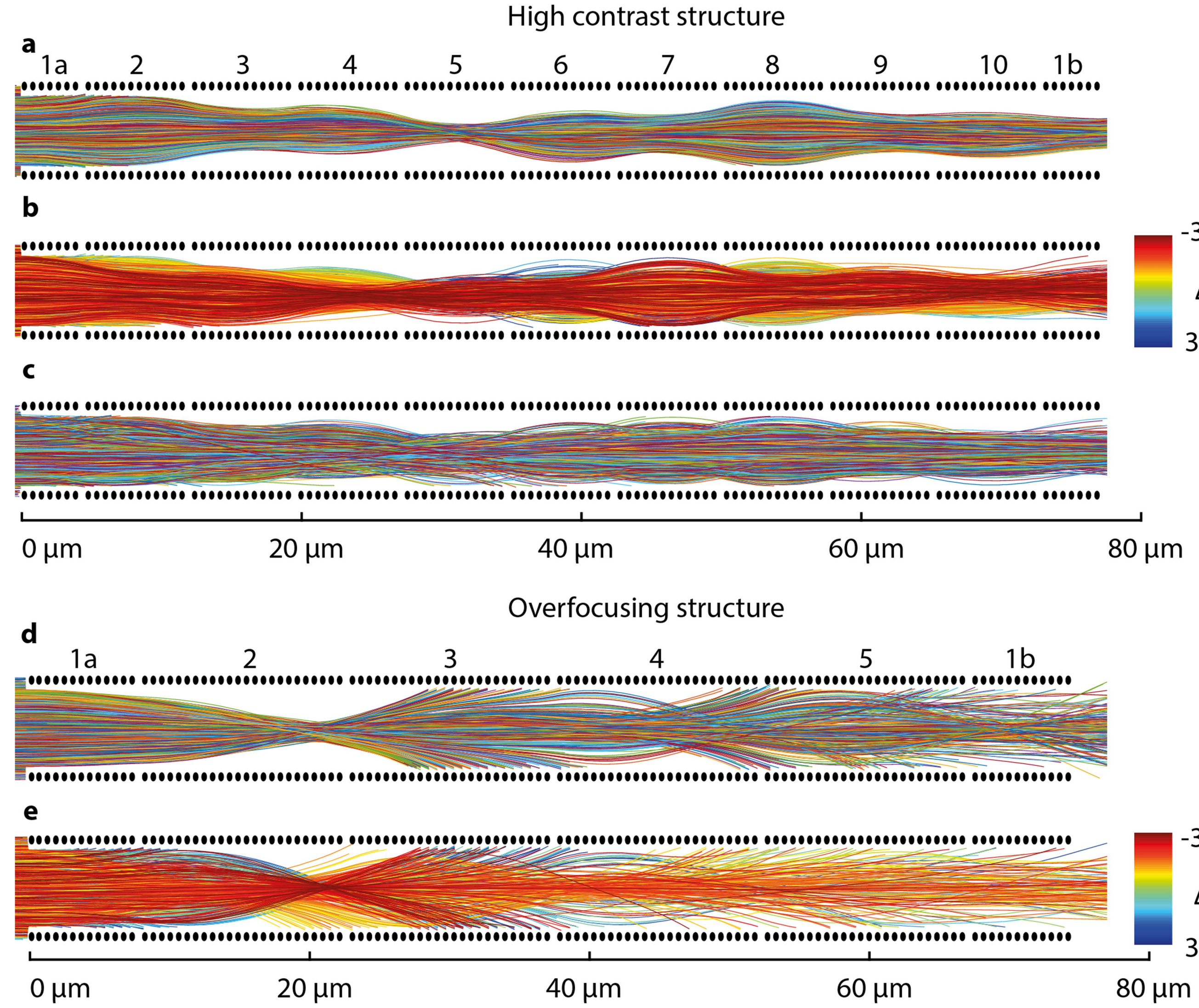

Extended Data Fig. 4 | Particle tracking simulation: One optical phase vs. all optical phases. (a) Example particle trajectories for the optimal guiding field strength. The differently colored curves in between the pillars denote individual particle trajectories. The APF behaviour is clearly visible in the breathing of the envelope of the particle trajectories. For illustrative purposes the simulation was conducted with an electron pulse length of 0.001 fs. This way, the APF effect is apparent because electrons only sample fields of a small random fraction of the optical cycle, away from the crest. The lattice periodicity of 2 × (7.149 µm + 0.589 µm) = 15.47 µm (see Fig. 3), which is equal to the beta function periodicity, can be directly seen in the envelope of the trajectories, where the phase jump is manifested as a bending of the curve. Hence we can here directly assign F to macro cell 2, D to macro cell 3, and so on repeatedly (see numbering at the top of each macro cell, macro cell 1 consists of 2 half cells at the beginning and the end of the structure). (b) Same as (a) but with all optical phases uniformly sampled. The electron pulse (flat-hat here) is one optical period long. Evidently, the existence of the two fixed points in phase, π/2 and 3π/2, cannot be easily discerned close to the entrance of the structure, meaning that F and D cannot be uniquely assigned to each cell. Halfway through the structure, however, the lattice oscillations become visible again in the form of two "modes", namely two trajectory classes, each directly linked to the lattice period again. The evolution into this two-mode structure is a consequence of the electrons accumulating around the two fixed points in phase space separated by π[13]. The result is an overlapping of two breathing motions in the trajectories shifted by one macro cell. (c) Same as (b) though the flat-hat electron pulse is here 400 fs long, the APF scheme still leads to particle propagation with hardly any loss, and the overall envelope nearly matches that of the single-cycle pulse in (b) (same as Fig. 4e of the main text). (d) Example particle trajectories with the over-focusing behaviour visible (same as Fig. 4f of the main text). Again, we only show particle trajectories of an electron pulse with a duration of 0.001 fs. Particles are obviously lost, where the lost particles' deviation from the design axis exceeds the aperture of the structure. (e) Same as in (d) but with all phases sampled. A similar effect as depicted in (b) takes place, where the loss of particles at the structure boundary occurs at multiple locations. The reason is, again, that macro cells act differently depending on where the electron is with respect to the optical phase, and hence experience forces shifted in phase. Most importantly, the overall performance of the APF scheme is maintained, if not for the limitation of the beam size due to the structure aperture. The colours in panels a, c, and d were chosen so individual trajectories can be better discerned. The colours in b and e indicate the injection time of the electron (see colour bar).